


# Integrated silicon-based suspended racetrack micro-resonator for biological solution sensing with high-order mode

Tao Ma(马涛), Yong-Sheng Tian(田永生), Shao-Hui Liu(刘少晖), Jia-He Ma(马家赫), Heng Liu(刘恒), and Fang Wang(王芳)

**Citation:**Chin. Phys. B, 2021, 30 (**11**): 114208. DOI: 10.1088/1674-1056/abf106
Journal homepage: http://cpb.iphy.ac.cn; http://iopscience.iop.org/cpb

**What follows is a list of articles you may be interested in**

---

## Design and fabrication of GeAsSeS chalcogenide waveguides with thermal annealing

Limeng Zhang(张李萌), Jinbo Chen(陈锦波), Jierong Gu(顾杰荣), Yixiao Gao(高一骁), Xiang Shen(沈祥), Yimin Chen(陈益敏), and Tiefeng Xu(徐铁峰)

Chin. Phys. B, 2021, 30 (**3**): 034210. DOI: 10.1088/1674-1056/abd757

## Polarization-independent silicon photonic grating coupler for large spatial light spots

Lijun Yang(杨丽君), Xiaoyan Hu(胡小燕), Bin Li(李斌), and Jing Cao(曹静)

Chin. Phys. B, 2021, 30 (**2**): 024206. DOI: 10.1088/1674-1056/abbc00

## Unitary transformation of general nonoverlapping-image multimode interference couplers with any input and output ports

Ze-Zheng Li(李泽正), Wei-Hua Han(韩伟华), Zhi-Yong Li(李智勇)

Chin. Phys. B, 2020, 29 (**1**): 014206. DOI: 10.1088/1674-1056/ab5783

## Characterize and optimize the four-wave mixing in dual-interferometer coupled silicon microrings

Chao Wu(吴超), Yingwen Liu(刘英文), Xiaowen Gu(顾晓文), Shichuan Xue(薛诗川), Xinxin Yu(郁鑫鑫), Yuechan Kong(孔月婵), Xiaogang Qiang(强晓刚), Junjie Wu(吴俊杰), Zhihong Zhu(朱志宏), Ping Xu(徐平)

Chin. Phys. B, 2019, 28 (**10**): 104211. DOI: 10.1088/1674-1056/ab3f9b

## Properties of metal-insulator-metal waveguide loop reflector

Hu Long(龙虎), Xuan-Ke Zeng(曾选科), Yi Cai(蔡懿), Xiao-Wei Lu(陆小微), Hong-Yi Chen(陈红艺), Shi-Xiang Xu(徐世祥), Jing-Zhen Li(李景镇)

Chin. Phys. B, 2019, 28 (**9**): 094215. DOI: 10.1088/1674-1056/ab38a3

---

# Integrated silicon-based suspended racetrack micro-resonator for biological solution sensing with high-order mode*

Tao Ma(马涛)[1,2,†], Yong-Sheng Tian(田永生)[1], Shao-Hui Liu(刘少晖)[1], Jia-He Ma(马家赫)[1], Heng Liu(刘恒)[1,3], and Fang Wang(王芳)[1,2]

[1] College of Electronic and Electrical Engineering, Henan Normal University, Xinxiang 453007, China
[2] Henan Key Laboratory of Optoelectronic Sensing Integrated Application, Xinxiang 453007, China
[3] Academician Workstation of Electromagnetic Wave Engineering of Henan Province, Xinxiang 453007, China

(Received 18 January 2021; revised manuscript received 19 March 2021; accepted manuscript online 23 March 2021)

A biological sensing structure with a high-order mode ($E_{21}^{y}$) is designed, which is composed of a suspended racetrack micro-resonator (SRTMR) and a microfluidic channel. The mode characteristics, coupling properties, and sensing performances are simulated by using the finite element method (FEM). To analyze the mode confinement property, the confinement factors in the core and cladding of the suspended waveguide for the $E_{11}^{x}$, $E_{11}^{y}$, and $E_{21}^{y}$ are calculated. The simulation results show that the refractive index (RI) sensitivity of the proposed sensing structure can be improved by using the high-order mode ($E_{21}^{y}$). The RI sensitivity for the $E_{21}^{y}$ mode is $\sim 201$ nm/RIU, which is twice to thrice higher than those for the $E_{11}^{x}$ mode and the $E_{11}^{y}$ mode. Considering a commercial spectrometer, the proposed sensing structure based on the SRTMR achieves a limit of detection (LOD) of $\sim 4.7 \times 10^{-6}$ RIU. Combined with the microfluidic channel, the SRTMR can possess wide applications in the clinical diagnostic assays and biochemical detections.

**Keywords:** micro-resonator, suspended racetrack, biological sensor, limit of detection

**PACS:** 42.82.–m, 42.79.Gn, 87.85.fk, 07.07.Df **DOI:** 10.1088/1674-1056/abf106

## 1. Introduction

Silicon is a main material for the design and fabrication of photonic integrated circuit (PICs) due to the complementary metal–oxide semiconductor (CMOS) compatibility.[1,2] Silicon-based photonic micro-resonators (MRs) have been widely investigated in various research fields, such as optical modulations, optical interconnects, wavelength convertors, nano-linear optics, THz technology, optical detections, and optical sensors.[3–9] Furthermore, the large refractive index (RI) difference of silicon-based waveguide can greatly reduce the cross section of waveguide to nanometer scale, which greatly reduces the amount of solution for detection. Hence, the silicon-based MRs are widely adopted as sensors which show great potential applications in the clinical diagnostic assays and biochemical detections. The silicon-based MRs including ring, disk, racetrack, toroids, have been widely investigated due to their remarkable enhancements of light-matter interaction and widespread applications in sensing, metrology and nonlinear optics.[10–15]

The racetrack micro-resonator (RTMR)-based sensors rely on the evanescent waves, which spread into the surrounding medium to detect the presence of solutions or molecules. The resonance characteristics and sensing performances of the RTMR-based sensor can be adjusted by flexibly controlling the coupling strength at the straight part in the RTMR. The improvement in sensitivity of the RTMR-based sensor depends mainly on loss, polarization, and the interaction between light and the surrounding medium. Recently, several different materials, composite structures, and polarization states have been investigated to enhance the sensitivity of the integrated RTMR. An RTMR with the quasi-TM guided mode is investigated for the RI and biological sensing. The design parameters are optimized to obtain the highest sensitivity ($\sim 270$ nm/RIU) with the help of the Multi-Project Wafer (MPW) foundries.[16] To enlarge the overlap between mode and the surrounding solution, silicon is replaced by silicon-oxy-nitride (SiON) for the core material.[17–19] The sensitivity of a single SiON-based RTMR is $\sim 434.94$ nm/RIU with an ultrahigh figure of merit (FOM) of $\sim 4.6 \times 10^{4}$ RIU$^{-1}$, and a dual SiON-based MR can greatly improve the limit of detection (LOD) which is $\sim 1.81\times^{-6}$ RIU. The porous silicon (PS)-based RTMRs are investigated for biosensing due to the advantages of the PS, such as the large internal surface and biocompatibility.[20,21] As a porous material, PS is a favorable host to various molecules and allows a direct interaction between the light and molecules to be detected. A theoretical sensitivity of 1170 nm/RIU is calculated, and the experimental results verify that a sensitivity of $\sim 560$ nm/RIU with a limit of detection of $\sim 8 \times 10^{-5}$ RIU is obtained. Combined with the subwavelength grating (SWG), an SWG-based RTMR is proposed for ultrasensitive sensing

*Project supported by the National Natural Science Foundation of China (Grant No. 62075057) and Ph. D. Program of Henan Normal University, China (Grant Nos. 5101239170010 and gd17167).

†Corresponding author. E-mail: matao@htu.edu.cn

© 2021 Chinese Physical Society and IOP Publishing Ltd 

with the TM mode.[22] The theoretical and experimental results demonstrate that a sensitivity of ∼ 429.74 nm/RIU and a limit of detection of $\sim 3.71 \times 10^{-4}$ RIU are achieved by optimizing the structure parameters. A T-shape suspended silicon nitride MR is experimentally demonstrated for an optical sensing with a sensitivity of ∼ 247 nm/RIU.[23] Compared with unsuspended sensing structures, the suspended MR enhances the interaction between light and the surrounding solutions. An RTMR sensor based on a plasmonic metal–insulator–metal (MIM) structure is designed, which achieves an RI sensitivity of ∼ 4650 nm/RIU and a temperature sensitivity of ∼ 0.33 nm/°C.[24] The plasmonic structure greatly reduces the size of the sensing device, which can break through the diffraction limit.

In this paper, a suspended racetrack micro-resonator (SRTMR) with a higher mode ($E_{21}^{y}$) is investigated by using the finite element method (FEM). Combined with the microfluid channel, an SRTMR-based sensor operating at ∼ 1550 nm can be achieved. The suspended structure can enlarge the overlap between light and the surrounding solutions to be detected, thus the sensing performances can be improved. The mode characteristics including effective refractive index and optical confinement factor are calculated with the two-dimensional (2D) mode analysis. Using the three-dimensional (3D) frequency-domain analysis, the sensing performances are investigated. The rest of this paper is organized as follows. In Section 2, the structure of the SRTMR and the analysis approach are demonstrated. In Section 3, the characteristics of the SRTMR including the mode characteristics, coupling properties, and transmission properties are analyzed and optimized. In Section 4, the sensing performances of the SRTMR-based sensor are studied. Conclusions are drawn in Section 5.

## 2. Structure model and method

The schematic of the silicon-based SRTMR is shown in Fig. 1(a). The suspended silicon layers (RI∼ 3.5) are etched above the bottom silica substrate (RI∼ 1.45). Considering the biological sensing applications, the surrounding dielectric of the silicon layer is set to be aqueous solution whose RI is ∼ 1.33. The cross-section (*xy* plane) of the SRTMR is shown in Fig. 1(b). As shown in Figs. 1(a) and 1(b). the bending radius and straight part length of the SRTMR are $R$ and $L_0$, respectively. The width and thickness of the waveguide are $w_0$ and $h_0$, respectively. The height of the suspended structure above the silica substrate is $h_1$. The gap between the bus waveguide and MR is $w_1$.

To evaluate the transmission performances of the SRTMR, the quality factor ($Q$) and extinction ratio ($ER$) are used, which can determine the spectral resolution and affect the sensing performances in the measurement of spectral shift.[25] The $Q$ factor can be calculated from[26]

$$Q = \lambda_{\mathrm{res}} / \Delta\lambda_{\mathrm{FWHM}}, \tag{1}$$

where $\lambda_{\mathrm{res}}$ is the resonant wavelength and $\Delta\lambda_{\mathrm{FWHM}}$ is the full width at half maximum of the resonant peak. And $ER$ is defined as

$$ER = -10\log_{10}\left(P_{2\mathrm{max}}/P_{2\mathrm{min}}\right), \tag{2}$$

where $P_{2\mathrm{max}}$ and $P_{2\mathrm{min}}$ are respectively the maximum value and minimum value of the output power from port 2 of the SRTMR.

The sensitivity of an SRTMR-based sensor is defined by the ratio between the wavelength shift ($\Delta\lambda_{\mathrm{res}}$) at the resonant peak and the change of the solution RI ($\Delta n_{\mathrm{c}}$) as follows:

$$S = \Delta\lambda_{\mathrm{res}} / \Delta n_{\mathrm{c}}, \tag{3}$$

where $\lambda_{\mathrm{res}}$ is the resonance wavelength of the resonance peak and $n_{\mathrm{c}}$ is the solution RI in the microfluidic channel. The sensitivity can be calculated by using the linear fitting.[27] The mode characteristics and sensing performances of the SRTMR will be investigated by the commercial software COMSOL Multiphysics based on the FEM which is widely used to simulate the characteristics of integrated photonic devices. The mode characteristics can be calculated by the 2D mode analysis, and the coupling properties, transmission properties, and sensing performances can be simulated by the 3D frequency domain analysis.

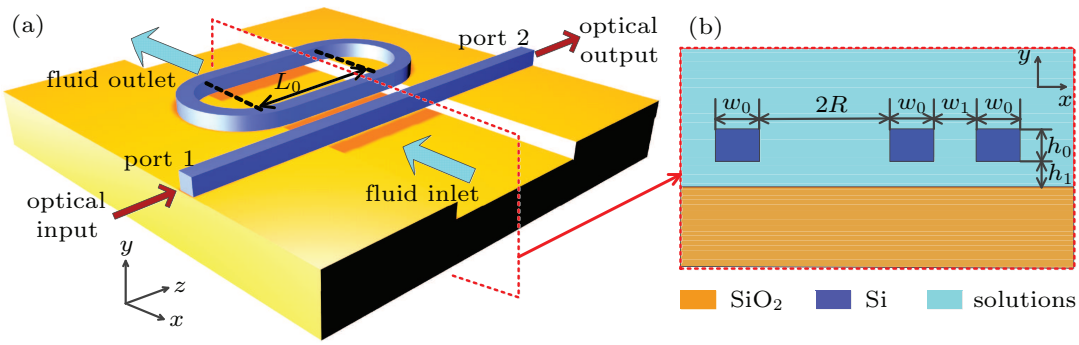



**Fig. 1.** Schematic diagram of suspended racetrack micro-resonator (SRTMR), showing (a) 3D model and (b) cross-section of coupling part.

## 3. Characterization of SRTMR

### 3.1. Mode characteristics

The mode effective RIs ($n_{\text{eff}}$) of the guided modes in the SRTMR with different values of $w_0$ and $h_0$ are shown in Figs. 2(a)–2(c) at an operating wavelength of 1550 nm, and the field distributions of two fundamental modes and three high-order modes are shown in Fig. 2(d). According to the Marcatili's method, the guided modes in a rectangular waveguide are classified as two groups: $\mathrm{E}^x_{mn}$ mode and $\mathrm{E}^y_{mn}$ mode, where $x$ and $y$ each represent the direction of electrical polarization, $m$ and $n$ are the numbers of the electric field maximum values along $x$ and $y$ axes. The $\mathrm{E}^x_{mn}$ mode and the $\mathrm{E}^y_{mn}$ mode are also known as quasi-TE and quasi-TM mode, respectively. The electrical polarization directions of the modes are shown by the black arrows in Fig. 2(d). As shown in Figs. 2(a)–2(c), the number of modes increases with $h_0$ increasing when $w_0$ remains unchanged. When $w_0$ and $h_0$ are chosen to be 400 nm and 350 nm, only the first three low-order modes ($\mathrm{E}^x_{11}$, $\mathrm{E}^y_{11}$, and $\mathrm{E}^y_{21}$) exist in the waveguide. The mode effective RIs increase sharply and then change slowly as $h_0$ increases. The modes will degenerate when $h_0$ and $w_0$ satisfy certain conditions.

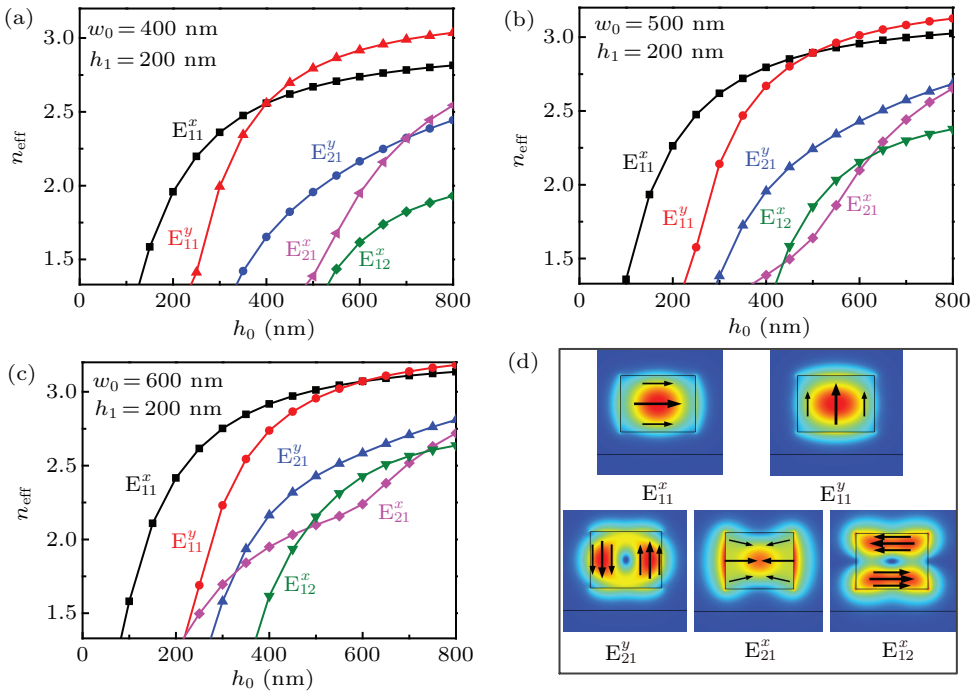



**Fig. 2.** Calculated mode effective RIs ($n_{\text{eff}}$) and field distributions of guided modes ($\mathrm{E}^x_{11}$, $\mathrm{E}^y_{11}$, $\mathrm{E}^y_{21}$, $\mathrm{E}^x_{21}$, and $\mathrm{E}^x_{12}$) *versus* $h_0$ at wavelength of 1550 nm when $h_1 = 200$ nm: $w_0 = 400$ nm (a), 500 nm (b), 600 nm (c), and (d) field distributions at $w_0 = 400$, $h_0 = 350$ nm, and $h_1 = 200$ nm.

In order to evaluate the optical field confinement, the confinement factor ($\Gamma$) is used, which is defined as[28]

$$\Gamma = \frac{n_{\mathrm{A}} c \varepsilon_0 \iint_A |\boldsymbol{E}|^2 \,\mathrm{d}x\mathrm{d}y}{\iint_\infty \mathrm{Re}\{\boldsymbol{E} \times \boldsymbol{H}^*\}) \cdot \hat{e}_z \mathrm{d}x\mathrm{d}y}, \tag{4}$$

where $n_{\mathrm{A}}$ is the RI in the confinement region to be measured, $c$ is the speed of light in vacuum, $\varepsilon_0$ is the permittivity of vacuum, $\boldsymbol{E}$ is the electric field, $\boldsymbol{H}^*$ is the complex conjugate of the magnetic field $\boldsymbol{H}$, and $\hat{e}_z$ is the polarization vector along the $z$ axis. The $\mathrm{Re}\{\boldsymbol{E} \times \boldsymbol{H}^*\}$ returns to the real part of $\boldsymbol{E} \times \boldsymbol{H}^*$.

The confinement factors of the core and cladding ($\Gamma_{\text{core}}$ and $\Gamma_{\text{cladding}}$) with different values of $w_0$, $h_0$, and $h_1$ are calculated and the results are shown in Figs. 3(a)–3(d). For the $\mathrm{E}^x_{11}$, $\mathrm{E}^y_{11}$, and $\mathrm{E}^y_{21}$ modes, $\Gamma_{\text{core}}$ increases with $h_0$ increasing from 150 nm to 800 nm, but $\Gamma_{\text{cladding}}$ changes in a reverse way. The $\Gamma_{\text{core}}$ increases but $\Gamma_{\text{cladding}}$ decreases when $w_0$ increases from 400 nm to 500 nm. In Fig. 3(a), $\Gamma_{\text{core}}$ is higher than 97.7%, and $\Gamma_{\text{cladding}}$ is less than 2.3% when $h_0$ is 800 nm. In Fig. 3(b), $\Gamma_{\text{core}}$ is higher than 95.2%, and $\Gamma_{\text{cladding}}$ is less than 4.8% when $h_0$ is 800 nm. In Fig. 3(c), $\Gamma_{\text{core}}$ is higher than 94.7%, and $\Gamma_{\text{cladding}}$ is less than 5.3% when $h_0$ is 800 nm. To enhance the interaction between the modes and surrounding solutions, it is necessary to choose the high $\Gamma_{\text{cladding}}$ and low $\Gamma_{\text{core}}$. Hence, the smaller $w_0$ and $h_0$ are the best options. But the smaller size of the waveguide will reduce the number of the guided modes in the suspended waveguide as shown in Figs. 2(a)–2(c). Considering a tradeoff between the above two, $w_0$ and $h_0$ are set to be 400 nm and 350 nm. In Fig. 3(d), $\Gamma_{\text{core}}$ and $\Gamma_{\text{cladding}}$ first increase and then hardly change with increase of $h_1$. Because the small $h_1$ results in more electric field energy entering into the silicon substrate. The influences of $h_1$ on $\Gamma_{\text{core}}$ and $\Gamma_{\text{cladding}}$ for the $\mathrm{E}^x_{11}$ and $\mathrm{E}^y_{11}$ modes are less than that for the $\mathrm{E}^y_{21}$ mode when $h_1$ is small. The $\Gamma_{\text{core}}$ and $\Gamma_{\text{cladding}}$ have no significant increase when $h_1$ is large. To enhance the interaction between the modes and surrounding solutions, $h_1$ is chosen to be 200 nm.

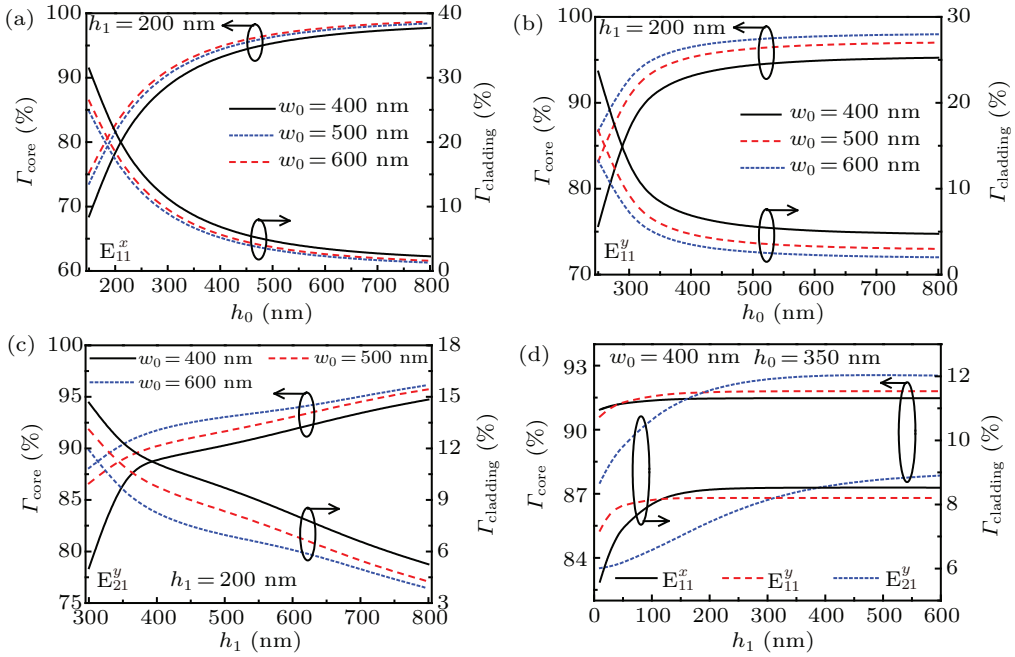



**Fig. 3.** Confinement factors in core and cladding *versus* $h_1$ of SRTMR with different values of $h_0$ and $w_0$ for (a) $\mathrm{E}_{11}^{x}$ mode, (b) $\mathrm{E}_{11}^{y}$ mode, and (c) $\mathrm{E}_{21}^{y}$ mode, and (d) confinement factors when $w_0 = 400$ nm and $h_0 = 350$ nm.

### 3.2. Coupling property

To demonstrate the coupling properties, the coupling section of the SRTMR is illustrated in Fig. 4(a). The $\mathrm{E}_{21}^{y}$ mode is excited from port 1 and output from port 2 and port 3. The influences of $L_0$ on the outputs of port 2 and port 3 are illustrated in Figs. 4(b) and 4(c). The normalized power of the outputs from port 2 and port 3 are defined as $T_2 = -10\log_{10}(P_2/P_1)$

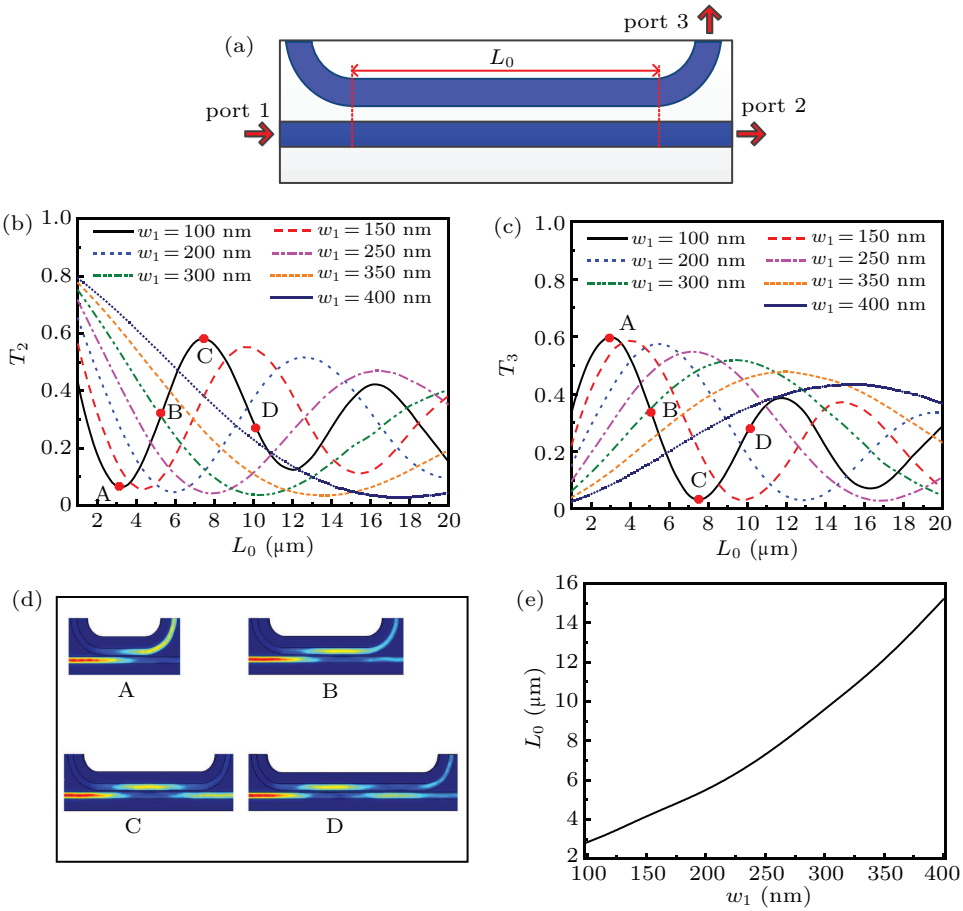



**Fig. 4.** (a) Coupling section of SRTMR, (b) normalized output power of port 2, (c) normalized output power of port 3, (d) field distributions of $\mathrm{E}_{21}^{y}$ mode at points A, B, C, and D, and (e) $L_0$ *versus* $w_1$.

and $T_3 = -10\log_{10}(P_3/P_1)$, respectively. Here, $P_1$, $P_2$, and $P_3$ are the power of port 1, port 2, and port 3, respectively. In the remaining simulations, $T_2$ is also used to calculate the transmission spectrum of the SRTMR, which is replaced by $T$. As shown in Figs. 4(b) and 4(c), $T_2$ and $T_3$ are periodic sine waves with reduced amplitude as $L_0$ increases. The $T_2$ has a minimum value and the $T_3$ has a maximum value when $L_0$ is $\sim 3$ μm (point A). The reverse happens when $L_0$ is $\sim 7$ μm (point C). The $T_2$ and $T_3$ are closely approximated when $L_0$ values are $\sim 5$ μm and $\sim 10$ μm (point B and point D). In Fig. 4(d), the electric field distributions for the $E_{21}^y$ mode are illustrated at points A, B, C, and D. As shown in Figs. 4(b) and 4(c), the cycles of $T_2$ and $T_3$ go up with the increase of $w_1$. The interaction length $L_0$ at the first maximum $T_3$ as a function of $w_1$ is shown in Fig. 4(e). The longer $L_0$ is necessary to obtain a maximum $T_3$ when $w_1$ increases.

### 3.3. Transmission properties

To study the transmission properties, the transmission spectra of the SRTMR for the $E_{11}^x$, $E_{11}^y$, and $E_{21}^y$ modes are simulated. The transmission spectrum from 1500 nm to 1600 nm is shown in Fig. 5(a) when $R = 2$ μm, $L_0 = 2.7$ μm, and $w_1 = 100$ nm. Using the Lorentz fit, four resonant peaks are achieved in the transmission spectrum from 1540 nm to 1570 nm as shown in Fig. 5(b). According to the field distributions of the modes, the peak 1 is the $E_{11}^x$ mode, the peak 2 is the $E_{21}^y$ mode, and the peak 3 and peak 4 are the $E_{11}^y$ mode, respectively. The influence of $w_1$ on $T$ is shown in Fig. 5(c) when $R$ =2 μm and $L_0 = 2.7$ μm. With the increase of $w_1$, the resonant peaks drop. The peak 1 is slightly blue-shifted, however the wavelength of peak 2 hardly changes. The peak 3 and peak 4 are significantly red-shifted and blue-shifted, respectively. When $w_1$ increase to 250 nm, the peak 3 and peak 4 overlap into one due to the mode degeneracy.

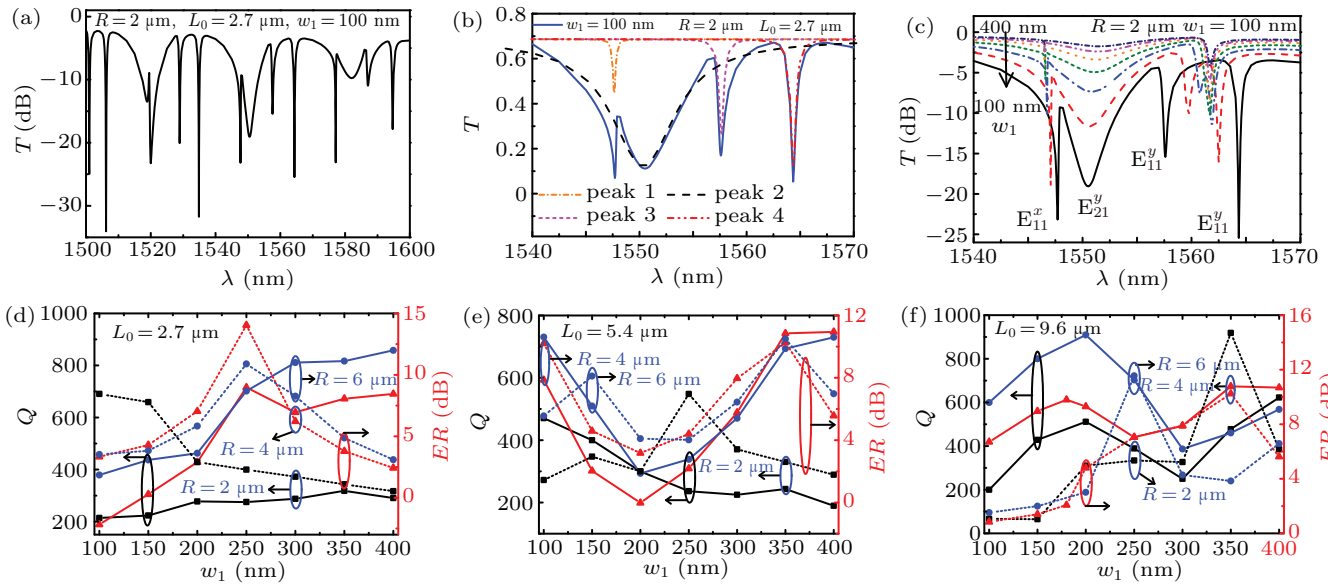



**Fig. 5.** (a) Transmission spectrum when $R = 2$ μm, $L_0 = 2.7$ μm, and $w_1 = 100$ nm, (b) fitting peaks of transmission spectrum, (c) transmission spectrum with different values of $w_1$, $Q$, and $ER$ with different values of $w_1$ when $L_0 = 2.7$ μm (d), 5.4 μm (e), and 9.6 μm (f).

The transmission spectra of the $E_{11}^x$ mode and the $E_{11}^y$ mode have been widely investigated. Here, we focus on the transmission response of $E_{21}^y$ mode. To explain the changes of $Q$ and $ER$, the critical coupling of the SRTMR is used which indicates that the internal loss of the resonator is equal to the coupling loss induced by the bus waveguide. Then, the SRTMR will be at under-coupling or over-coupling state when the internal loss is greater or smaller than the coupling loss. Figures 5(d)–5(f) show $Q$ and $ER$ with different values of $R$, $L_0$, and $w_1$. In Fig. 5(d), $Q$ increases but $ER$ decreases with the increase of $w_1$ when $R$ is 2 μm and $L_0$ is 2.7 μm. The critical coupling condition is satisfied when $w_1$ is $\sim 100$ nm. However, the coupling loss decreases when $w_1$ increases, which breaks the critical condition. The SRTMR goes into the under-coupling state and results in the decrease of $ER$. When $R$ increases to 4 μm and 6 μm, the internal losses in the SRTMR increase, and the critical conditions are broken. The SRTMR is at the over-coupling state with a small $w_1$ due to the high coupling loss. In order to return to the critical coupling state, the coupling loss should be reduced. As shown in Figs. 4(b) and 4(c), $T_2$ increases and $T_3$ decreases with the increase of $w_1$ when $L_0 = 2.7$ μm, which reduces the coupling losses. Hence, the SRTMR reaches the critical state again when $w_1$ increases to $\sim 250$ nm and $ER$ has a maximum value. As shown in Figs. 4(b) and 4(c), $T_2$ has a minimum value and $T_3$ has a maximum value when $L_0 =\sim 5.4$ μm and $w_1 =\sim 200$ nm. The corresponding coupling loss is the biggest, and the resonator is at over-coupling state. Therefore, there are smaller ERs when $w_1$ is $\sim 200$ nm as shown in Fig. 5(e). When $w_1$ increases or decreases from 200 nm, $T_2$ increases and the corresponding

coupling losses decreases as shown in Fig. 4(b). The SRTMR reaches the critical coupling state, whether $w_1$ increases or decreases from 200 nm. When $R = 2$ μm, the critical coupling state occurs when $w_1$ values are ∼ 150 nm and ∼ 250 nm. The critical coupling states of the SRTMR with $R$ values of 4 μm and 6 μm are achieved when $w_1$ values are ∼ 100 nm and ∼ 350 nm, respectively. Owing to the periodic changes of $T_2$ and $T_3$ with $w_1$, the changes of $ER$ and $Q$ are more complex when $L_0$ is 9.6 μm as shown in Fig. 5(f). The SRTMR is in the over-coupling state when $w_1$ is ∼ 300 nm. When $w_1$ increases from 300 nm, $T_2$ increase monotonically. Hence, the critical coupling state of the SRTMR occurs when $w_1$ is larger than 350 nm. The $Q$ has a maximum value when $w_1$ is ∼ 170 nm but $ER$s have no maximum values. Because $T_3$ does not linearly change when $w_1$ is less than 300 nm. The $Q$ can be improved when the SRTMR goes into the under-coupling state from the over-coupling state, which can be achieved by reducing the coupling loss or increasing the internal loss.

## 4. Sensing performances

In applications, the sensing structure based on an SRTMR can be designed as shown in Fig. 6. The SRTMR is immersed in the flowing solution which is injected into the microfluidic channel from the fluid inlet.[29] Meanwhile, the probe optical signal can be coupled into (out of) the optical input (output) of the bus waveguide from (into) an optical fiber via an in-plane grating coupler.[30] The solutions with different RIs ($n_c$ values) are pumped into a fluid reservoir, and flow along the microfluidic channel through the suspended micro-racetrack into another fluid reservoir. Here, the RI ($n_c$) value of the biological and chemical solutions both vary from 1.33 to 1.41.

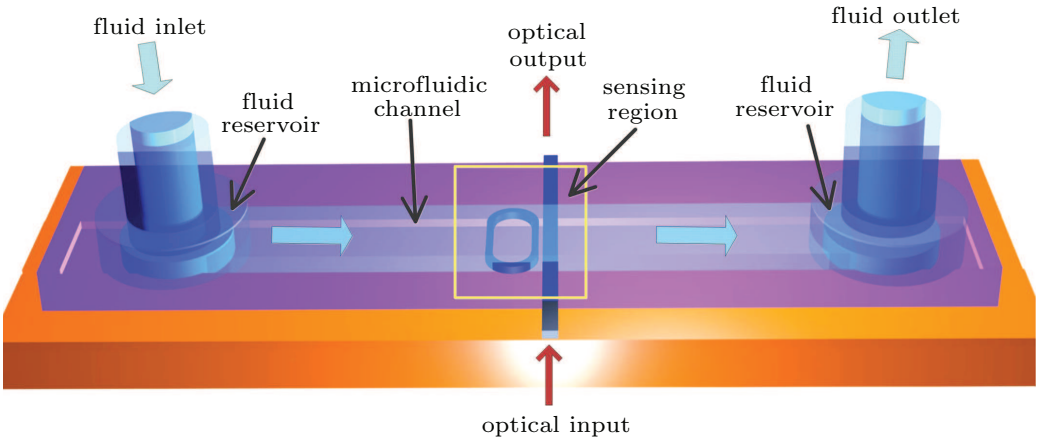



**Fig. 6.** Schematic diagram of sensing structure based on SRTMR combined with microfluidic channel.

The SRTMR can be fabricated on an SOI wafer by using the standard CMOS technique and nanoimprint technique.[30,31] To fabricate a partly suspended structure, an additional etching for the silica substrate should be carried out under being carefully controlled.[32–34] The SRTMR can be sealed with a pre-fabricated flexible microfluidic channel.[35] The microfluidic channels can be fabricated with polyethylene (PE), polypropylene (PP), polydimethylsiloxane (PDMS), SU-8, and PMMA, which can ensure fluidic confinement within the channels, easy interconnection with external microfluidic control devices, simple and inexpensive fabrication, and good ability to handle a variety of specimen sizes from biological applications.[36–40]

The transmission spectra of the $E_{21}^y$ mode with various values of $n_c$ and $L_0$ for $R = 4$ μm are shown in Figs. 7(a), 7(c), and 7(e). The transmission spectra are significantly red-shifted as $n_c$ increases from 1.33 to 1.41. The extinction ratio of the resonant peak significantly decreases with $n_c$ because the SRTMR goes into the under-coupling state from the critical coupling state when $L_0 = 2.7$ and 5.4 μm. When $L_0$ is 9.6 μm, $ER$ increases with $n_c$ increasing due to the periodic changes of $T_2$ and $T_3$. The resonant wavelengths as a function of $n_c$ and the linear fittings are shown in Figs. 7(b), 7(d), and 7(f). The RI sensitivities with different values of $L_0$ and $R$ are shown in Fig. 7(g). The highest sensitivity of 201 nm/RIU can be achieved when $R = 4$ μm and $L_0 = 2.7$ μm. For comparison, the sensitivities of the suspended micro-racetrack resonator ($R = 4$ μm and $L_0 = 5.4$ μm) with the $E_{11}^x$ mode and the $E_{11}^y$ mode are also shown in Fig. 7(g). The sensitivity with the $E_{21}^y$ mode is twice to thrice higher than those with the $E_{11}^x$ and $E_{11}^y$ modes.

In addition to $S$, the limit of detection (LOD) is another important performance indicator, which is defined as[41]

$$\mathrm{LOD} = \delta\lambda / S, \tag{5}$$

where $\delta\lambda$ is the resolution of a spectrometer, which characterizes the smallest possible spectral shift for accurate measurement. For a commercial spectrometer, $\delta\lambda$ is ∼ 0.001 nm. The sensor based on the SRTMR achieves an LOD of ∼ $4.7 \times 10^{-6}$ RIU. The RI sensing performances of the sensing structures based different racetrack resonators are listed in Table 1.

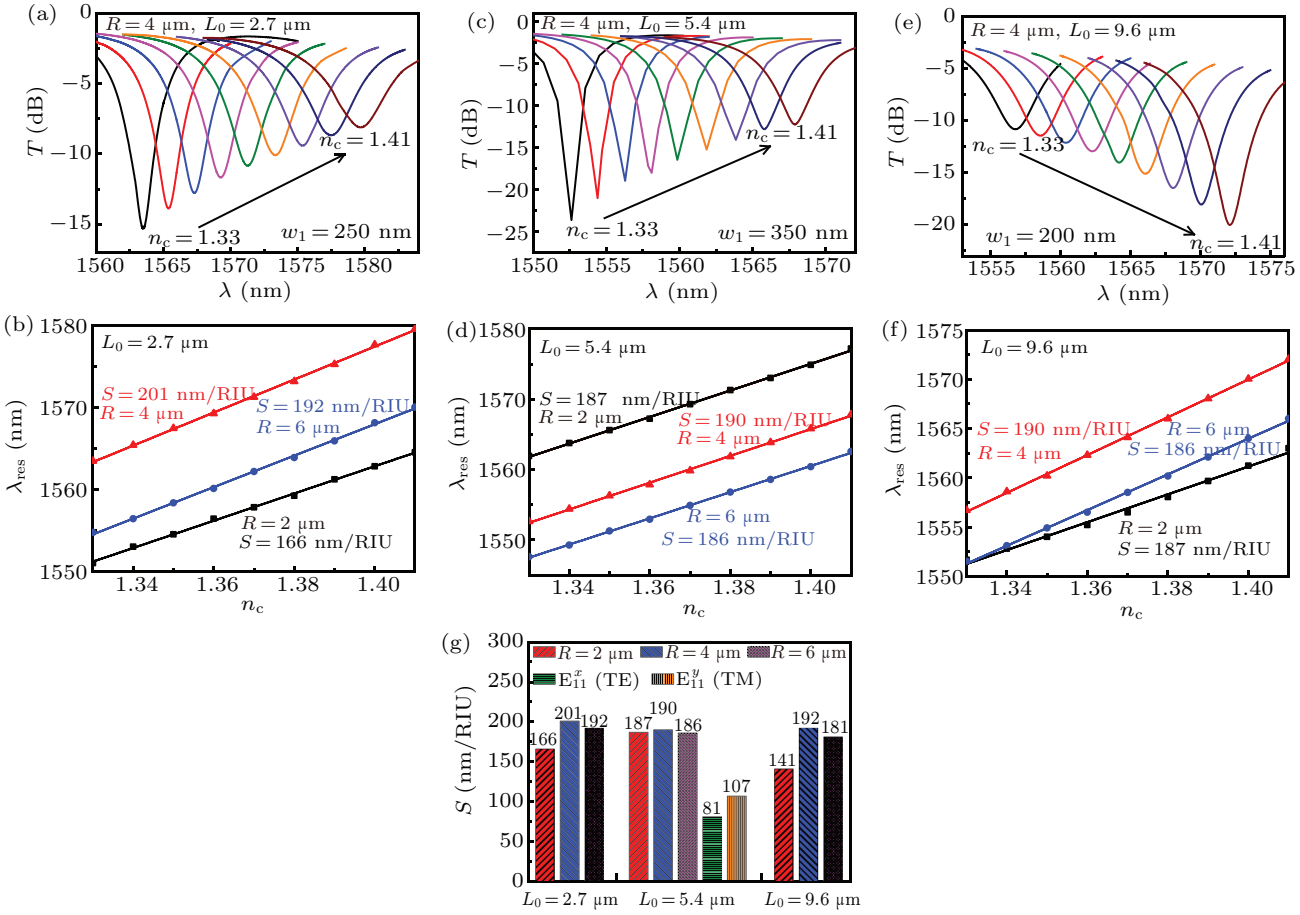



**Fig. 7.** Sensing performances of SRTMR, transmission spectra of $E_{21}^{y}$ mode with different values of $n_c$ at a fixed $R$ of 4 μm and $L_0 = 2.7$ μm (a), 5.4 μm (c), 9.6 μm (e), the changes of $\lambda$ with $n_c$ at $L_0 = 2.7$ μm (b), 5.4 μm (d), 9.6 μm (f), and RI sensitivity contrast (g).

**Table 1.** Comparison of RI and temperature sensing performances among different configurations.

| Materials | Modes@$\lambda_{res}$ (nm) | Waveguide size | $R$ (μm) | $L_0$ (μm) | $S$ (nm/RIU) | $n_c$ | LOD (RIU) | Refs. |
|---|---|---|---|---|---|---|---|---|
| SOI | TM@∼1550 | $650 \times 165$ nm$^2$ | 40 | 13.15 | 270 | 1.333–1.343 | $\sim 1.2 \times 10^{-3}$ | [16] |
| Silicon | $E_{21}^{y}$@∼1550 | $400 \times 350$ nm$^2$ | 4 | 2.7 | 201 | 1.33–1.41 | $\sim 4.7 \times 10^{-6}$ | [this work] |
| Silicon | TM@∼1550 | $600 \times 220$ nm$^2$ | 10 | 6.5 | 429.7 | 1.333–1.362 | $\sim 3.71 \times 10^{-4}$ | [22] |
| Porous silicon | TE@∼1550 | $1.9 \times 1.8$ μm$^2$ | 100 | 70 | 560 | $\Delta n_c = 1.7 \times 10^{-3}$ | $\sim 7.9 \times 10^{-5}$ | [20] |
| Porous silicon | TM@∼1550 | $1.8 \times 2.5$ μm$^2$ | 70 | 25 | 1170 | 1.369–1.374 | $\sim 1.5 \times 10^{-4}$ | [21] |
| SiON | TM@∼850 | $1.0 \times 0.24$ μm$^2$ | 40 | 100 | 112 | $\Delta n_c = 6 \times 10^{-4}$ | $\sim 1.6 \times 10^{-6}$ | [42] |
| SiON | TE@∼850 | $1.0 \times 0.3$ μm$^2$ | 100 | 35 | 80 | $\Delta n_c = 8 \times 10^{-4}$ | $\sim 3 \times 10^{-6}$ | [43] |
| SiON | TE@∼850 | 1-μm width | 19 | 35 | 435 | $\Delta n_c = 1.37 \times 10^{-4}$ | $\sim 4.27 \times 10^{-5}$ | [19] |
| SiON | TE@∼850 | 1-μm wide | 19 | 35 | 434.94 | 1.332–1.352 | $\sim 4.21 \times 10^{-5}$ | [17] |
| Silicon nitride | TE@∼1550 | $1.3 \times 0.31$ μm$^2$ | 20 | 40 | 247 | 1.316–1.364 | $\sim 6.3 \times 10^{-4}$ | [23] |
| $SiO_xN_y$ | TE@∼850 | $1.0 \times 0.22$ μm$^2$ | 90 | 35 | 84 | 1.330–1.481 | $\sim 1.48 \times 10^{-4}$ | [18] |
| Gold on cytop | plasomic mode@∼1550 | $5.0 \times 0.04$ μm$^2$ | 50 | 50 | 1200 | 1.32–1.34 | $\sim 8 \times 10^{-7}$ | [44] |
| Ag-air-Ag | plasomic mode@∼5000 | 50-nm width | ∼0.3 | 0.04 | 4650 | 1–1.1 | $\sim 4.3 \times 10^{-2}$ | [24] |

## 5. Conclusions

In summary, a biological sensing structure based on the SRTMR is designed for biological sensing. To improve the sensitivity, the suspended structure with high-order mode ($E_{21}^{y}$) is studied. By using the finite element method (FEM), the coupling property and sensing performances are simulated. The simulation results show that the RI sensitivity of the sensor based on the SRTMR is ∼ 201 nm/RIU. The sensitivity for the $E_{21}^{y}$ mode is twice to thrice higher than those for the $E_{11}^{x}$ and $E_{11}^{y}$ modes. The limit of detection is $\sim 4.7 \times 10^{-6}$ RIU when a commercial spectrometer is used. In order to achieve flexible biochemical sensing, a microfluidic channel is combined with the SRTMR, which can have potential applications in the clinical diagnostic assays and biochemical detections.

## References

[1] Novack A, Streshinsky M, Ding R, Liu Y, Lim A E, Lo G, Baehr-Jones T and Hochberg M 2014 *Nanophotonics* **3** 205

[2] Selvaraja S K, Bogaerts W, Dumon P, Van Thourhout D and Baets R 2010 *IEEE J. Sel. Top. Quant.* **16** 316
[3] Xu X, Jin X, Gao H, Cheng J, Lu Y, Chen D and Yu L 2020 *Acta Phys. Sin.* **69** 184207 (in Chinese)
[4] Guo J and Dai D 2018 *Chin. Phys. B* **27** 104208
[5] Wang Z, Liu H, Sun Q, Huang N, Li S and Han J 2016 *J. Laser Phys.* **26** 075403
[6] Ariannejad M M, Akbari E, Thong P Y, Ghasemi M, Dehzangi A and Ahmad H 2019 *Eur. Phys. J. D* **73** 176
[7] Xie J, Zhu X, Zang X, Cheng Q, Chen L and Zhu Y 2018 *Opt. Mater. Express* **8** 50
[8] Tyler N A, Barreto J, Villarreal-Garcia G E, Bonneau D, Sahin D, O'Brien J L and Thompson M G 2016 *Opt. Express* **24** 8797
[9] Zhou X, Liu L, Xu W, Song B, Sheng J, He M and Shi H 2015 *Sci. Rep.* **4** 4572
[10] Van Eeghem A, Werquin S, Hoste J W, Goes A, Vanderleyden E, Bienstman P and Dubruel P 2017 *Appl. Surf. Sci.* **405** 321
[11] Xiao T, Yu Y and Li Z 2017 *Acta Phys. Sin.* **66** 217802 (in Chinese)
[12] Vahala K J 2003 *Nature* **424** 839
[13] Boyd R W and Heebner J E 2001 *Appl. Opt.* **40** 5742
[14] Yang S, Wang Y and Sun H 2015 *Adv. Opt. Mater.* **3** 1136
[15] Meng L, Wang M, Shen Y, Yang Y, Xu W, Zhang L and Wang K 2020 *Acta Phys. Sin.* **69** 014203 (in Chinese)
[16] Fard S T, Schmidt S, Shi W, Wu W, Jaeger N A F, Kwok E, Ratner D M and Chrostowski L 2017 *Biomed. Opt. Express* **8** 500
[17] Khozeymeh F and Razaghi M 2018 *J. Opt. Soc. Am. B* **35** 2734
[18] Khozeymeh F and Razaghi M 2019 *Phys. Rev. Appl.* **12** 054045
[19] Khozeymeh F and Razaghi M 2018 *IEEE Sens. J.* **19** 1299
[20] Girault P, Azuelos P, Lorrain N, Poffo L, Lemaitre J, Pirasteh P, Hardy I, Thual M, Guendouz M and Charrier 2017 *J. Opt. Mater.* **72** 596
[21] Girault P, Lorrain N, Lemaitre J, Poffo L, Guendouz M, Hardy I, Gadonna M, Gutierrez A, Bodiou L and Charrier 2015 *J. Opt. Mater.* **50** 167
[22] Huang L, Yan H, Xu X, Chakravarty S, Tang N, Tian H and Chen R T 2017 *Opt. Express* **25** 10527
[23] Feng J and Akimoto R 2015 *IEEE Photon. Technol. Lett.* **27** 1601
[24] Rakhshani M R andMansouri-Birjandi M A 2018 *Photon. Nanostruct.* **32** 28
[25] Ciminelli C, Campanella C M, Dell Olio F, Campanella C E and Armenise M N 2013 *Prog. Quant. Electron.* **37** 51
[26] Bogaerts W, De Heyn P, Van Vaerenbergh T, De Vos K, Kumar Selvaraja S, Claes T, Dumon P, Bienstman P, Van Thourhout D and Baets R 2012 *Laser Photon. Rev.* **6** 47
[27] Luan E, Yun H, Laplatine L, Dattner Y, Ratner D M and Cheung K C 2019 *IEEE J. Sel. Top. Quant.* **25** 7300211
[28] Robinson J T, Preston K, Painter O and Lipson M 2008 *Opt. Express* **16** 16659
[29] Xu D X, Vachon M, Densmore A, Ma R, Janz S, Delage A, Lapointe J, Cheben P, Schmid J H and Post E 2010 *Opt. Express* **18** 22867
[30] Bogaerts W, Baets R, Dumon P, Wiaux V, Beckx S, Taillaert D, Luyssaert B, Van Campenhout J, Bienstman P and Van Thourhout D 2005 *J. Lightwave Technol.* **23** 401
[31] Chou S Y, Krauss P R and Renstrom P J 1996 *Science* **272** 85
[32] Burek M J, Chu Y, Liddy M S Z, Patel P, Rochman J, Meesala S, Hong W, Quan Q, Mikhail M D, Lukin D and Lončar M 2014 *Nat. Commun.* **5** 5718
[33] Zhang R, Sun J, Chen G, Cheng M and Jiang J 2017 *Appl. Phys. Lett.* **111** 031102
[34] Chen P, Zhu Y, Shi Y, Dai D and He S 2012 *Opt. Express* **20** 22531
[35] Wang C, Quan Q, Kita S, Li Y and Lončar M 2015 *Appl. Phys. Lett.* **106** 261105
[36] Hu X, Xu G, Wen L, Wang H, Zhao Y, Zhang Y, Cumming D R S and Chen Q 2016 *Laser Photon. Rev.* **10** 962
[37] Watts B R, Zhang Z, Xu C, Cao X and Lin M 2012 *Biomed. Opt. Express* **3** 2784
[38] Densmore A, Vachon M, Xu D X, Janz S, Ma R, Li Y H, Lopinski G, Delage A, Lapointe J, Luebbert C C, Liu Q Y, Cheben P and Schmid J H 2009 *Opt. Lett.* **34** 3598
[39] Gervinskas G, Day D J and Juodkazis S 2012 *Opt. Mater. Express* **2** 279
[40] Soltani M, Lin J, Saraf S N, Forties R A, Lipson M and Wang M *in CLEO:* 2013 *San Jose, California: Optical Society of America*, 2013, p. AM4M.3
[41] White I M and Fan X 2008 *Opt. Express* **16** 1020
[42] Guider R, Gandolfi D, Chalyan T, Pasquardini L, Samusenko A, Pucker G, Pederzolli C and Pavesi L 2015 *Sensors* **15** 17300
[43] Samusenko A, Gandolfi D, Pucker G, Chalyan T, Guider R, Ghulinyan M and Pavesi L 2016 *J. Lightwave Technol.* **34** 969
[44] Voronin K V, Stebunov Y V, Voronov A A, Arsenin A V and Volkov V S 2020 *Sensors* **20** 203